Applied Computing and Geosciences 23 (2024) 100172

Contents lists available at ScienceDirect

Applied Computing and Geosciences

journal homepage: www.sciencedirect.com/journal/applied-computing-and-geosciences

Computational fluid dynamics in carbonate rock wormholes using magnetic resonance images as structural information

Gustavo Solcia *, Bernd U. Foerster, Mariane B. Andreeta, Tito J. Bonagamba, Fernando F. Paiva

São Carlos Institute of Physics, University of São Paulo, São Carlos, SP, Brazil

ARTICLE INFO

Keywords:
Wormhole
MRI
CFD

ABSTRACT

Computational fluid dynamics (CFD) is an essential tool with growing applications in many fields. In petrophysics, it is common to use computed tomography in those simulations, but in medicine, magnetic resonance imaging (MRI) is also being used as a basis for structural information. Wormholes are high-permeability structures created by the acidification of carbonate reservoirs and can impact reservoir production. CFD combined with MRI can benefit the study of wormholes in petrophysics, but combining both techniques is still a challenge. The objective of this study is to develop a pipeline for performing CFD in wormholes with MRI data. Using three samples of carbonate rocks acidified with 1.5% hydrochloric acid at 0.1, 1, and 10 ml/min, we acquired 300 μm resolution T2-weighted images and experimental measurements of pressure data within flow rates of 5 to 50 ml/min. We applied cropping, bias field correction, non-local means denoising, and segmentation in the image processing step. For the 3D reconstruction, we used marching cubes to generate the surface mesh, the Taubin filter for surface smoothing, and boundary modeling with Blender. Finally, for the CFD, we generated volumetric meshes with cfMesh and used the OpenFOAM simpleFoam solver to simulate an incompressible, stationary, and laminar flow. We analyzed the effect of surface smoothing, estimating edge displacements, and measured the simulation pressure at the same flow rates as the experiments. Surface smoothing had a negligible impact on the overall edge position. For most flow rates, the simulation and experimental pressure measurements matched. A possible reason for the discrepancies is that we did not consider the surrounding porous media in the simulations. In summary, our work had satisfactory results, demonstrating CFD's feasibility in studying wormholes using MRI.

1. Introduction

Computational fluid dynamics (CFD) has many applications in industry (Johnson et al., 2005; Johnson, 1996; Liou and Povinelli, 2013; Runchal, 2013) and in the field of medicine (Chung and Cebral, 2015; Kim et al., 2010; Miller et al., 2021; Primeaux et al., 2021). Some applications of CFD in medicine use magnetic resonance imaging (MRI), which could also benefit petrophysics for understanding flows in rocks.

The acidification of carbonate oil reservoirs creates structures with dissolution patterns that can increase oil production due to their high permeability. The structures produced by the acidification of oil carbonate reservoirs are called wormholes, and the dissolution patterns depend on the acidification procedure (Dong et al., 2018; dos Santos Lucas et al., 2023). The injection flow rate is an essential factor in acidification, and a better understanding of flows inside wormholes could bring light to desirable wormhole features. Creating different wormhole patterns in laboratory samples with sizes that fit computed tomography or pre-clinical MRI scanners is possible.

Commonly, studies of CFD in porous media use computed tomography (CT) data as a basis for structural information (Appoloni et al., 2007; Palma et al., 2019; Mostaghimi et al., 2012; Neumann et al., 2021). However, there is a great motivation to use MRI for porous media imaging. MRI is a powerful imaging method that uses the signal from the Hydrogen nuclei from the confined liquid (water in this case). That is particularly interesting for porous media and wormhole imaging because it is possible to reconstruct the volume that is reachable by the water (the effective porosity). Also, in comparison to CT, MRI provides more contrast options (Symms et al., 2004) and the possibility of carrying out dynamic studies.

Many current CFD simulations that involve wormholes study the dissolution process (Soulaine and Tchelepi, 2016). However, the simulation of dissolution networks lies outside the scope of this study. Unlike simulations in the literature on carbonate dissolution, we are interested in better understanding the flow in wormholes in a controlled environment after acidification. Therefore, MRI can be a valuable tool in

* Corresponding author.
E-mail address: gustavo.solcia@usp.br (G. Solcia).

https://doi.org/10.1016/j.acags.2024.100172
Received 21 July 2023; Received in revised form 2 January 2024; Accepted 10 June 2024
Available online 18 June 2024

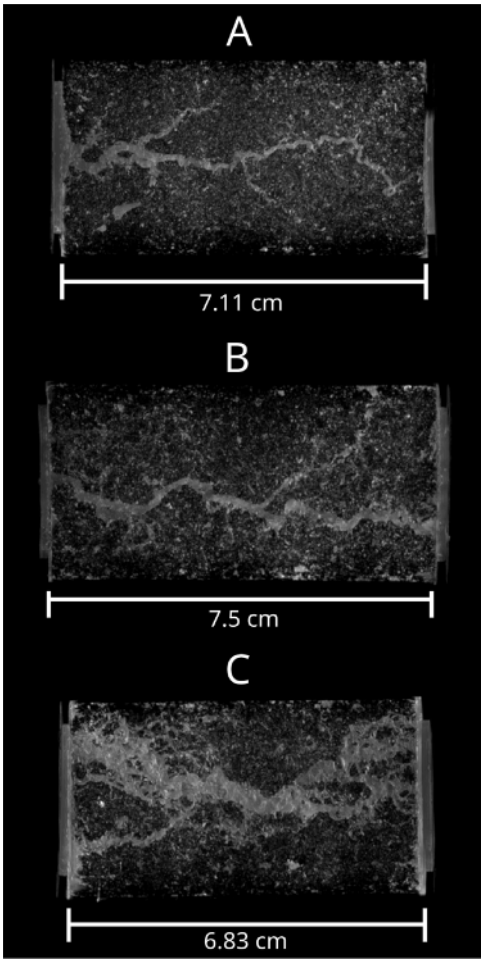

Fig. 1. Maximum intensity projection (MIP) of mirrored free induction steady precession (PSIF) from acidified carbonates. Samples A, B, and C were acidified with 0.1, 1, and 10 ml/min, respectively, to create distinct wormhole patterns. The wormholes are bright and continuous structures extending from the top of samples to the bottom.

this scenario. Performing simulations with structural data as the ones already established with CT is a first step to exploring the possibilities with MRI. However, its pipeline lies in the development of the image protocol and the image processing algorithms, which are the main bottlenecks for a representative simulation.

The objective of this study is to propose a pipeline to perform CFD simulations in wormholes using MRI data as a basis for structural information. As a specific objective, we aim at developing a robust methodology and investigating the validity of the simulations by comparing the results with pressure experiments.

2. Methodology

2.1. Experimental setup

The Petrobras Research Facility Centro de Pesquisas Leopoldo Americo Miguel de Mello (CENPES) provided three cylindrical samples of carbonate rocks acidified with 1.5% hydrochloric acid at different flow rates. Each sample was a by-product of the same piece of Indiana Limestone rock with a length of about 7.0 cm and a diameter of 3.8 cm. The carbonates received acid injections at 0.1, 1, and 10 ml/min to create different patterns of wormholes, which we named A, B, and C, respectively. For additional petrophysical information, CENPES also provided the porosity and permeability for each sample, as seen in Table 1.

Table 1
Geometrical and petrophysical information from acidified Indiana Limestone rock samples.

	A	*B*	*C*
Length (cm)	7.110	7.496	6.836
Diameter (cm)	3.795	3.800	3.807
Porosity (%)	17.10	17.00	16.96
K_{N2} (mD) (%)	545	465	465

Magnetic resonance images were acquired to visualize each wormhole structure. Samples were initially submerged in de-ionized water until complete saturation at a relative pressure of −650 mmHg for one hour. We used a thermal retractable material and a Teflon cover to seal the samples and prevent evaporation or mechanical flow loss during imaging acquisition. We then acquired T_2-weighted images so the contrast for wormholes had higher grayscale values. In that condition, T_2 from the confined water in the porous media is proportional to the pore size (Barrie, 2000) and consequently has lower grayscale values, promoting a better wormhole visualization. To obtain T_2-weighted images, we applied a 3D gradient echo sequence called mirrored free induction steady precession (PSIF) (Gyngell, 1988) with 300 μm isotropic resolution and a protocol that took five hours with TE = 4.5 ms, TR = 10.5 ms, excitation angle of 40 degrees, and 64 averages. Fig. 1 shows the resulting maximum intensity projection (MIP). The MRI equipment consisted of a 2T horizontal superconductor magnet from Oxford Instruments (model 85310 HR), a Bruker Avance III spectrometer (Bruker BioSpin, Inc., Billerica, MA, USA), and a homemade solenoid coil.

After image acquisition, we performed pressure measurements using an in-house built flow control system coupled with a High-Performance Liquid Chromatography (HPLC) pump (PU-4087, JASCO Corporation, Tokyo, Japan) that generated stable flow rates with 1% precision within 5–50 ml/min. The saturation process was repeated using cylindrical extensions of thermal retractile material connected to the flow control system. The pressure was measured as the water column height difference between the sample inlet and outlet, and the conversion assumed 10 m = 1 bar for de-ionized water.

3. Simulation pipeline

We applied many algorithms, divided into subsequent blocks, to maximize the fidelity of the geometric model based on MRIs. Fig. 2 shows the pipeline for image processing, 3D reconstruction, and CFD.

In the standardization step, we applied image cropping and bias field correction (Tustison et al., 2010). Image cropping removed the water trapped between the rocks and the Teflon cap. As the image size decreases, another benefit of image cropping is reducing computational processing time. The bias field correction from the Advanced Normalization Tools (ANTs) library reduced low-frequency variations in image intensity due to magnetic field inhomogeneities.

We applied a Non-local Means (NLM) algorithm modified to Rician noise in the image denoising step (Wiest-Daesslé et al., 2008). For magnitude images, the Rician noise distribution is a consequence of the modulus operation of real and imaginary parts with Gaussian noise. The filter was modified by cloning the scikit-image NLM denoising directory, substituting voxel restoration equations, and using the pseudo-residual technique to estimate noise variance (Gasser et al., 1986). We chose an h parameter value close to Coupé et al. (2012) optimization with $h = 1.15\sigma$, where σ is the noise variance, and we found a patch size of 5 and a patch distance of 6 to be a good trade-off between denoising and feature preservation.

Segmentations generally use statistical or threshold-based methods. Because most threshold methods are user dependent, we decided to use the Atropos k-means algorithm (Avants et al., 2011) from the ANTs library. We found that using three classes is the best option for wormhole

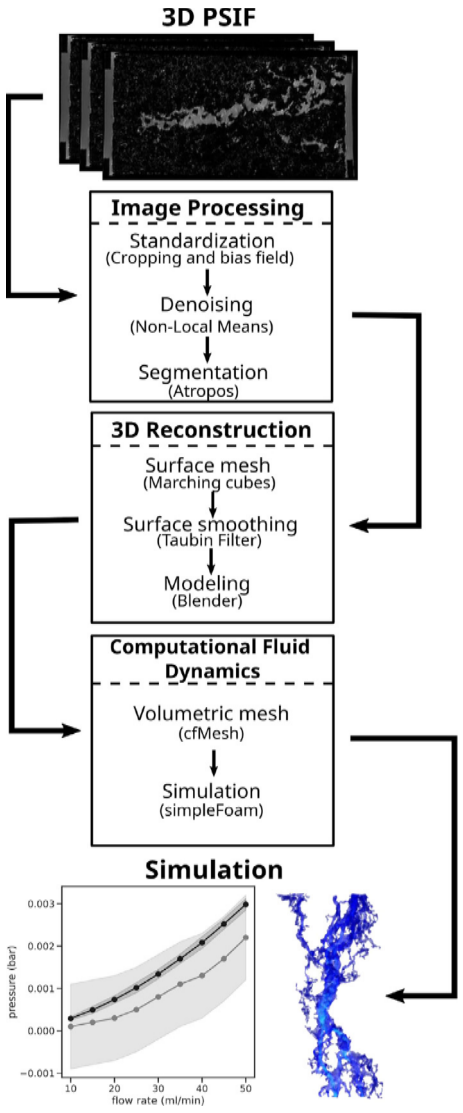

Fig. 2. Pipeline to create CFD simulations exemplified with velocity field and post-processing pressure measurements for a given flow rate. Image processing, 3D reconstruction, and CFD are the pipeline blocks.

segmentation. After extracting a binary image from the segmentation, we applied the marching cubes algorithm (Lorensen and Cline, 1987). The marching cubes were responsible for the 3D reconstruction, but the resulting surface still had sharp edges. The Taubin filter (Taubin, 1995) was then applied to smooth the surface while preserving the wormhole channel gauge. To test this assumption, we compared the displacement of edges between pre-and post-smoothing data using MeshLab software. We used marching cubes and the Taubin filter from The Visualization Toolkit (VTK) Python library. We applied the Blender software in the final step of the 3D reconstruction for boundary modeling and artifact removal. We created cylindrical extensions on the wormhole boundaries to emulate the experimental setup coupled with the HPLC pump. The extension had 3.8 cm in diameter and lengths of 5 cm and 23 cm, respectively, for the inlet and outlet to ensure flow stability.

The previous steps can be employed to create a surface mesh used in many CFD or mesh-generation software to obtain a volumetric mesh. We chose to work with the OpenFOAM (Weller et al., 1998) variant from OpenCFD Ltd. due to incorporating the mesh generation library called cfMesh in version v1712. CfMesh simplifies the volumetric mesh creation for the OpenFOAM environment. We used three cell sizes for each sample for a mesh independence analysis as described in Celik et al. (2008). In addition to the maximum cell size parameter, we used fixed values of 0.1 cm for the boundary cell size and refinement thickness with six additional refinement levels exclusively for the wormhole wall. We repeated the Blender modeling step with the necessary surface adjustment in the case of skew faces indicated in the mesh quality test. We adjusted the surfaces as many times as necessary to ensure that the mesh did not affect the continuity or convergence of the simulations.

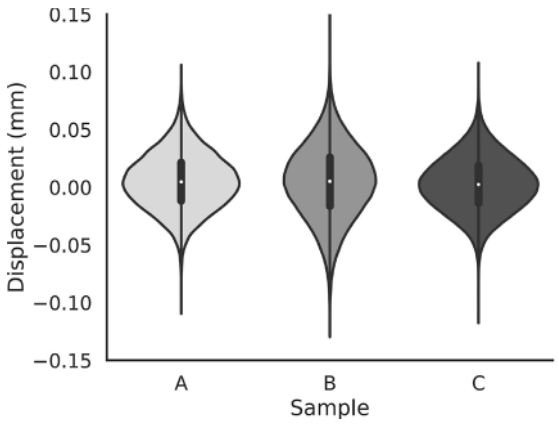

Fig. 3. Surface edges displacement from pre- and post-smoothing surfaces of wormholes samples.

In terms of fluid dynamics modeling, the simpleFoam solver was used to simulate an incompressible, stationary, and laminar flow. The simulation boundary conditions were based on experimental HPLC pump flow rates, ranging from 5 to 50 ml/min. These flow rates were applied with a parabolic velocity profile on the inlet boundary, following the Hagen–Poiseuille derivation. The pressure difference between the inlet and outlet was measured using OpenFOAM post-processing tools to compare simulated and experimental pressures. The mesh independence analysis calculated discretization error bars in simulated pressures. We used the software Paraview (Ahrens et al., 2005) volumetric rendering with the algorithm ZSWEEP for visualization and analysis of the velocity fields. Finally, we used Paraview and MeshLab to export velocity fields and calculate outlet cross-section areas to investigate the observed flow rates and velocity fields.

4. Results

The surface smoothing step during the 3D reconstruction can impact the position of edges and the overall shape of our wormhole samples. Then, we analyzed the displacement between surface mesh edges before and after smoothing, as shown in Fig. 3. Most of the measured displacements were within one-third of the voxel resolution range, with interquartile ranges of 0.033, 0.042, and 0.033 mm, and medians of 0.0046, 0.0052, and 0.0024 mm for samples A, B, and C, respectively.

The smooth surface models were attached to the flow extensions, and Fig. 4 shows the final model. The extensions positioning considered the orientation of the wormhole inside the sample. For each sample, volumetric meshes in three cell sizes used the same surface, as shown in Table 2. For every refinement, the total number of cells increased from A to B and B to C. Refinement factors satisfy the mesh independence analysis conditions (Celik et al., 2008).

Fig. 5 shows the simulation pressure results with flow rates ranging from 5 to 50 ml/min. With the cfMesh parameters described in the last section, we could perform the simulations in three mesh resolutions for the mesh independence analysis, resulting in discretization error estimates represented as the dark gray area. The light gray area represents the experimental uncertainty. From samples A to C, the pressure decays approximately one order of magnitude in the same flow rate range. Sample A revealed a difference between simulation and experimental

Table 2
Maximum cell size parameters used to generate volumetric meshes with the respective number of cells and refinement factors.

		A	B	C
Max cell size (cm)	C1	1	1	0.75
	C2	0.5	0.5	0.52
	C3	0.34	0.28	0.32
Number of cells	N1	788 180	826 402	1 484 263
	N2	2 001 856	2 680 970	3 301 038
	N3	4 513 921	7 484 287	9 666 472
Refinement factor	r21	1.36	1.48	1.31
	r32	1.31	1.41	1.43

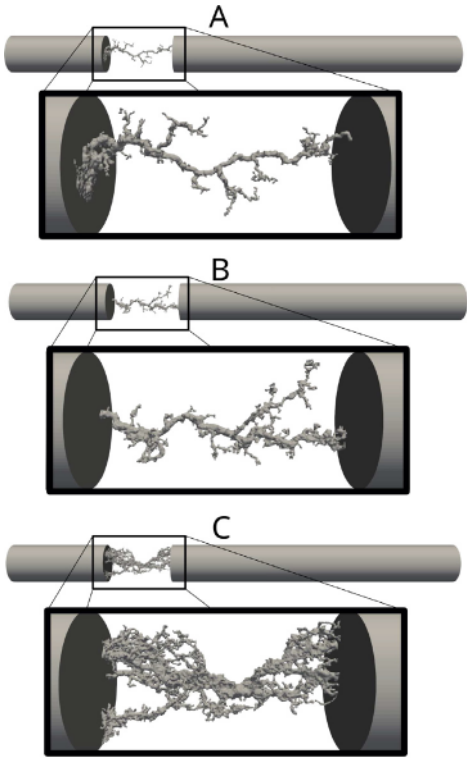

Fig. 4. Final surface model of the samples with inlet and outlet extensions. The zoomed regions show details of the structure of the wormhole.

pressures with flow rates starting at 30 ml/min. The right side of the pressure plots shows the magnitude of the velocity field in 50 ml/min flow rate for each sample. We observed higher magnitude values for sample A, followed by samples B and C.

We investigated the behavior of the observed velocity field and measured the pressure for a given flow rate analyzing the velocity magnitude at the main flow direction and the outlet cross-section from our samples. Fig. 6 shows the normalized velocity distribution for each sample with inserts of the respective outlet cross-section at a flow rate of 50 ml/min. Arrows indicate regions with distinct patterns of velocity distributions between the samples. Sample A has a wider distribution and reaches the highest velocities but with an outlet cross-section of 0.8 mm^2. Sample B's distribution reaches smaller velocities than sample A but has an outlet cross-section of 6.3 mm^2. Finally, sample C is the thinnest distribution and reaches the smaller velocities but has a total outlet cross-section of 15.2 mm^2.

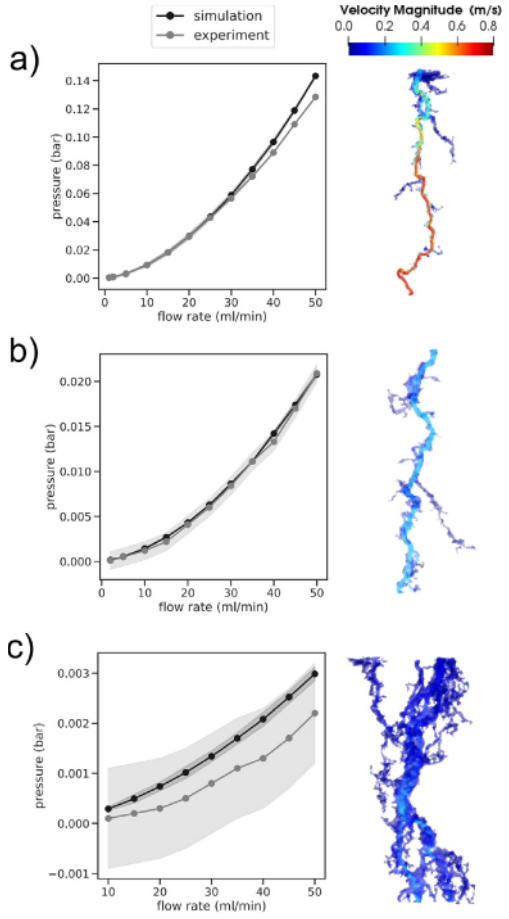

Fig. 5. Pressure versus flow rate for experimental and simulation measurements. Velocity magnitude field at 50 ml/min on the right side of the subfigures. (A) Sample A acidified with the injection of 0.1 ml/min. (B) Sample B acidified with the injection of 1 ml/min. (C) Sample C acidified with the injection of 10 ml/min.

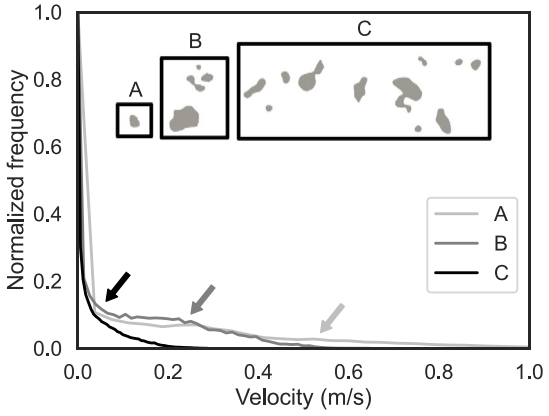

Fig. 6. Normalized distribution of velocity magnitude on main flow direction from samples A, B, and C at 50 ml/min flow rate. Arrows highlight different velocities patterns between distributions in their respective line colors. The inserts show outlet cross-sections for each sample.

5. Discussion

In this study, we have shown a pipeline to perform CFD simulations using MRI data. MRI for wormhole imaging has the advantage of a contrast determined by the confined fluid. Our choices of cropping, bias field correction, NLM denoising, and Atropos segmentation were

to maximize fidelity for MRI data. The need for cropping, bias field correction, and denoising depends on the quality or type of the data. On the other hand, segmentation is crucial, and one must favor a user-independent algorithm.

For complex structures such as wormholes, surface smoothing facilitates the meshing process but causes displacements that can potentially affect the original structure of the object. Evaluation of the displacement before and after smoothing revealed a negligible impact on the overall edge position compared to a voxel resolution of 300 μm. The center of the violin plot distributions was close to zero, and the interquartile ranges and most of the displacements within a third of the voxel resolution indicate that we achieved a smooth surface and preserved the wormhole channel gauge. It is important to emphasize that other artifacts from image acquisition or poor water saturation can have a more significant impact than the observed displacement because these artifacts impact the voxel's intensity and, consequently, the segmentation. The Taubin filter was designed to smooth without shrinkage; however, other algorithms could be applied if the edge displacement is analyzed carefully.

The importance of using extensions on the final surface model is two-fold. First, the extension length guarantees a well-conditioned flow for measurements at the boundaries, especially for the outlet. Also, when considering the wormhole alignment inside the samples, the extensions emulate the experimental measurements environment.

Generating three different volume mesh refinements makes applying the mesh independence analysis possible. The benefit of using the mesh independence analysis is to estimate the error from our simulations. Comparing experimental and simulation pressure values over multiple scales made it essential to use such error estimates in our study.

Higher flow rates in sample A have different pressures between simulation and experiments. This difference could be due to the influence of adjacent porous media on pressure measurements, which were not considered in our simulation model. However, most experimental pressure measurements are consistent with CFD results and validate the established pipeline. An exciting aspect of the velocity field data was its inverse relation to the outlet cross-section area from the samples. These velocity and area values can explain why sample C has the lowest pressure values to achieve a specific flow rate. One potential application of our results would be a flow analysis of wormhole patterns in more complex simulations, such as transient or multiphase flow.

Our results were focused on the flow in wormholes after acidification and aimed at using MRI as a tool for structure analysis at the core scale. MRI has multiple contrast options, and we choose to work with one specific for improving the structural contrast for the wormhole. Simulations of carbonate dissolution are a fundamental problem in the literature, with CT and simulated samples being the best way to address calculations. However, in addition to using MRI for the structural information of simulations, in the future, techniques such as 4D phase contrast MRI could have an essential role in further validating dynamics at the core scale. Therefore, our pipeline can help the simulation dynamics in wormholes and bridge the gap between dissolution simulations and experiments.

6. Conclusions

A pipeline to perform CFD simulations in wormholes from MRI data was shown. We acquired the data, applied image processing, and 3D reconstruction algorithms for creating volumetric mesh and performing simulations using OpenFOAM. Our samples were three cylindrical carbonate rocks acidified with 1.5% hydrochloric acid at 0.1, 1, and 10 ml/min. Surface smoothing from 3D reconstruction algorithms did not affect the geometry of samples. Flow extensions and mesh independence analysis plays an important role, respectively, for fidelity of the model and error estimation. The simulation and experimental pressure measurements were similar for most samples, with flow rates within 5 to 50 ml/min. However, sample A higher-end flow rates were an exception, and the reason could be that we did not consider the surrounding porous media in the simulations. Despite limitations due to not modeling the adjacent porous media, our work had satisfactory results demonstrating the feasibility of CFD on wormholes using MRI. These results provide a significant first step toward studying flow rates inside wormholes, being the foundations for more complex simulations and establishing MRI as an essential technique for porous media CFD. Future studies should consider transient and multiphase simulations.

CRediT authorship contribution statement

Gustavo Solcia: Writing – original draft, Software, Methodology, Investigation. **Bernd U. Foerster:** Software, Methodology, Data curation. **Mariane B. Andreeta:** Resources, Methodology. **Tito J. Bonagamba:** Project administration, Funding acquisition, Conceptualization. **Fernando F. Paiva:** Writing – review & editing, Supervision, Conceptualization.

Declaration of competing interest

The authors declare that they have no known competing financial interests or personal relationships that could have appeared to influence the work reported in this paper.

Data availability

Data will be made available on request.

Acknowledgments

Authors acknowledge the support of the following Brazilian Institutions: University of São Paulo (USP), Coordenação de Aperfeiçoamento de Pessoal de Nivel Superior, Brazil (CAPES, 88887.476130/2020-00), São Paulo Research Foundation, Brazil (FAPESP, 2009/54880-6, 2013/23740-0), Centro de Pesquisa e Desenvolvimento Leopoldo Américo Miguez de Mello, Brazil (CENPES/Petrobras, 2015/00416-8) and National Council for Scientific and Technological Development, Brazil (CNPq, 308076/2018-4, 425346/2018-8). Authors also acknowledge Carlos Speglich for his contributions and support to this research project.

Computer code availability

wormholeCFD

Contact: gustavo.solcia@usp.br; +5516997771540.

Hardware requirements: The code was developed on a computer with 6 CPU cores (3.7 GHz each) and 32 GiB RAM.

Program language: Python, C++.

Software required: OpenFOAM.

Program size: 39.2 MB.

The source codes used in the pipeline described in the paper are available for downloading at the link:

https://github.com/GustavoSolcia/wormholeCFD.

References

Ahrens, J., Geveci, B., Law, C., 2005. ParaView: An end-user tool for large-data visualization. In: Visualization Handbook. http://dx.doi.org/10.1016/B978-012387582-2/50038-1.

Appoloni, C.R., Fernandes, C.P., Rodrigues, C.R., 2007. X-ray microtomography study of a sandstone reservoir rock. Nucl. Instrum. Methods Phys. Res. Sect. A: Accel. Spectrom. Detect. Assoc. Equip. 580, 629–632. http://dx.doi.org/10.1016/j.nima.2007.05.027.

Avants, B.B., Tustison, N.J., Wu, J., Cook, P.A., Gee, J.C., 2011. An open source multivariate framework for N-tissue segmentation with evaluation on public data. Neuroinformatics 9, 381–400. http://dx.doi.org/10.1007/s12021-011-9109-y.

Barrie, P.J., 2000. Characterization of porous media using NMR methods. Ann. Rep. NMR Spectrosc. 41, http://dx.doi.org/10.1016/s0066-4103(00)41011-2.

Celik, I.B., Ghia, U., Roache, P.J., Freitas, C.J., Coleman, H., Raad, P.E., 2008. Procedure for estimation and reporting of uncertainty due to discretization in CFD applications. J. Fluids Eng. Trans. ASME 130, 0780011–0780014. http://dx.doi.org/10.1115/1.2960953.

Chung, B., Cebral, J.R., 2015. CFD for evaluation and treatment planning of aneurysms: Review of proposed clinical uses and their challenges. Ann. Biomed. Eng. 43, 122–138. http://dx.doi.org/10.1007/s10439-014-1093-6.

Coupé, P., Manjón, J.V., Robles, M., Collins, D.L., 2012. Adaptive multiresolution non-local means filter for three-dimensional magnetic resonance image denoising. IET Image Process. 6, 558–568. http://dx.doi.org/10.1049/iet-ipr.2011.0161.

Dong, K., Zhu, D., Hill, A.D., 2018. Mechanism of wormholing and its optimal conditions: A fundamental explanation. J. Pet. Sci. Eng. 169, 126–134. http://dx.doi.org/10.1016/j.petrol.2018.05.060.

dos Santos Lucas, C.R., Neyra, J.R., Araújo, E.A., da Silva, D.N.N., Lima, M.A., Ribeiro, D.A.M., Aum, P.T.P., 2023. Carbonate acidizing – a review on influencing parameters of wormholes formation. J. Pet. Sci. Eng. 220, 111168. http://dx.doi.org/10.1016/j.petrol.2022.111168, URL https://www.sciencedirect.com/science/article/pii/S0920410522010208.

Gasser, T., Sroka, L., Jennen-Steinmetz, C., 1986. Residual variance and residual pattern in nonlinear regression. Biometrika 73, http://dx.doi.org/10.1093/biomet/73.3.625.

Gyngell, M.L., 1988. The application of steady-state free precession in rapid 2DFT NMR imaging: FAST and CE-FAST sequences. Magn. Res. Imaging 6, http://dx.doi.org/10.1016/0730-725X(88)90478-X.

Johnson, N., 1996. The legacy and future of computational fluid dynamics at Los Alamos. In: Proceedings of the 1996 Canadian CFD Conference, vol. 836.

Johnson, F.T., Tinoco, E.N., Yu, N.J., 2005. Thirty years of development and application of CFD at boeing commercial airplanes, seattle. Comput. & Fluids 34, 1115–1151. http://dx.doi.org/10.1016/j.compfluid.2004.06.005.

Kim, H.J., Vignon-Clementel, I.E., Coogan, J.S., Figueroa, C.A., Jansen, K.E., Taylor, C.A., 2010. Patient-specific modeling of blood flow and pressure in human coronary arteries. Ann. Biomed. Eng. 38, http://dx.doi.org/10.1007/s10439-010-0083-6.

Liou, M.-S., Povinelli, L.A., 2013. Computational fluid dynamics: NASA Glenn research center's legacy and contributions. J. Aerosp. Eng. 26, 277–287. http://dx.doi.org/10.1061/(asce)as.1943-5525.0000295.

Lorensen, W.E., Cline, H.E., 1987. Marching cubes: A high resolution 3D surface construction algorithm. In: Proceedings of the 14th Annual Conference on Computer Graphics and Interactive Techniques. SIGGRAPH 1987, pp. 163–169. http://dx.doi.org/10.1145/37401.37422.

Miller, C., Padmos, R.M., van der Kolk, M., Józsa, T.I., Samuels, N., Xue, Y., Payne, S.J., Hoekstra, A.G., 2021. In silico trials for treatment of acute ischemic stroke: Design and implementation. Comput. Biol. Med. 137, http://dx.doi.org/10.1016/j.compbiomed.2021.104802.

Mostaghimi, P., Bijeljic, B., Blunt, M.J., 2012. Simulation of flow and dispersion pore-space images. SPE J. 17, 1131–1141. http://dx.doi.org/10.2118/135261-PA.

Neumann, R.F., Barsi-Andreeta, M., Lucas-Oliveira, E., Barbalho, H., Trevizan, W.A., Bonagamba, T.J., Steiner, M.B., 2021. High accuracy capillary network representation in digital rock reveals permeability scaling functions. Sci. Rep. 11, http://dx.doi.org/10.1038/s41598-021-90090-0.

Palma, P.R.D., Guyennon, N., Parmigiani, A., Huber, C., Hebe, F., Romano, E., 2019. Impact of synthetic porous medium geometric properties on solute transport using direct 3D pore-scale simulations. Geofluids 2019, http://dx.doi.org/10.1155/2019/6810467.

Primeaux, J., Salavitabar, A., Lu, J.C., Grifka, R.G., Figueroa, C.A., 2021. Characterization of post-operative hemodynamics following the norwood procedure using population data and multi-scale modeling. Front. Physiol. 12, http://dx.doi.org/10.3389/fphys.2021.603040.

Runchal, A.K., 2013. Emergence of computational fluid dynamics at imperial college (1965–1975): A personal recollection. J. Heat Transfer 135, http://dx.doi.org/10.1115/1.4007655.

Soulaine, C., Tchelepi, H.A., 2016. Micro-continuum approach for pore-scale simulation of subsurface processes. Transp. Porous Media 113, http://dx.doi.org/10.1007/s11242-016-0701-3.

Symms, M., Jäger, H.R., Schmierer, K., Yousry, T.A., 2004. A review of structural magnetic resonance neuroimaging. J. Neurol. Neurosurg. Psychiat. 75, 1235–1244. http://dx.doi.org/10.1136/jnnp.2003.032714.

Taubin, G., 1995. Curve and surface smoothing without shrinkage. In: IEEE International Conference on Computer Vision. pp. 852–857. http://dx.doi.org/10.1109/iccv.1995.466848.

Tustison, N.J., Avants, B.B., Cook, P.A., Zheng, Y., Egan, A., Yushkevich, P.A., Gee, J.C., 2010. N4ITK: Improved N3 bias correction. IEEE Trans. Med. Imaging 29, 1310–1320. http://dx.doi.org/10.1109/TMI.2010.2046908.

Weller, H.G., Tabor, G., Jasak, H., Fureby, C., 1998. A tensorial approach to computational continuum mechanics using object-oriented techniques. Comput. Phys. 12, 620. http://dx.doi.org/10.1063/1.168744.

Wiest-Daesslé, N., Prima, S., Coupé, P., Morrissey, S.P., Barillot, C., 2008. Rician noise removal by non-local means filtering for low signal-to-noise ratio MRI: Applications to DT-MRI. In: Lecture Notes in Computer Science (Including Subseries Lecture Notes in Artificial Intelligence and Lecture Notes in Bioinformatics), vol. 5242 LNCS, pp. 171–179. http://dx.doi.org/10.1007/978-3-540-85990-1_21.